



LJMU Research Online

Graef, F, Vukosavljevic, B, Michel, J-P, Wirth, M, Ries, O, De Rossi, C, Windbergs, M, Rosilio, V, Ducho, C, Gordon, S and Lehr, C-M

The bacterial cell envelope as delimiter of anti-infective bioavailability - An in vitro permeation model of the Gram-negative bacterial inner membrane.

<http://researchonline.ljmu.ac.uk/id/eprint/6677/>

Article

Citation (please note it is advisable to refer to the publisher's version if you intend to cite from this work)

Graef, F, Vukosavljevic, B, Michel, J-P, Wirth, M, Ries, O, De Rossi, C, Windbergs, M, Rosilio, V, Ducho, C, Gordon, S and Lehr, C-M (2016) The bacterial cell envelope as delimiter of anti-infective bioavailability - An in vitro permeation model of the Gram-negative bacterial inner membrane.

LJMU has developed [LJMU Research Online](#) for users to access the research output of the University more effectively. Copyright © and Moral Rights for the papers on this site are retained by the individual authors and/or other copyright owners. Users may download and/or print one copy of any article(s) in LJMU Research Online to facilitate their private study or for non-commercial research. You may not engage in further distribution of the material or use it for any profit-making activities or any commercial gain.

The version presented here may differ from the published version or from the version of the record. Please see the repository URL above for details on accessing the published version and note that access may require a subscription.

For more information please contact researchonline@ljmu.ac.uk

<http://researchonline.ljmu.ac.uk/>

1 **The Bacterial Cell Envelope as Delimiter of Anti-Infective Bioavailability – An *In Vitro***
2 **Permeation Model of the Gram-Negative Bacterial Inner Membrane**

3
4 Florian Graef^a, Branko Vukosavljevic^a, Jean-Philippe Michel^b, Marius Wirth^c, Oliver Ries^c,
5 Chiara De Rossi^a, Maike Windbergs^a, Véronique Rosilio^b, Christian Ducho^c, Sarah Gordon^{a*}
6 and Claus-Michael Lehr^{a,d*}
7
8

9 ^a Helmholtz Institute for Pharmaceutical Research Saarland (HIPS), Helmholtz Center for
10 Infection Research (HZI), Department of Drug Delivery, Campus E8 1, 66123 Saarbrücken,
11 Germany

12 E-mail: Florian.Graef@helmholtz-hzi.de, Branko.Vukosavljevic@helmholtz-hzi.de, Maike.
13 Windbergs@helmholtz-hzi.de, Chiara.DeRossi@helmholtz-hzi.de,
14 Sarah.Gordon@helmholtz-hzi.de, Claus-Michael.Lehr@helmholtz-hzi.de

15 ^b Institut Galien Paris Sud, UMR 8612, Univ Paris-Sud, CNRS, Université Paris-Saclay, 5 rue
16 J.B. Clément, F-92290 Châtenay-Malabry, France

17 E-Mail: jean-philippe.michel@u-psud.fr, veronique.rosilio@u-psud.fr

18 ^c Saarland University, Department of Pharmacy, Pharmaceutical and Medicinal Chemistry,
19 Campus C2 3, 66123 Saarbrücken, Germany

20 E-Mail: marius.wirth@uni-saarland.de, christian.ducho@uni-saarland.de

21 ^d Saarland University, Department of Pharmacy, Biopharmacy and Pharmaceutical
22 Technology, Campus E8 1, 66123 Saarbrücken, Germany

23 * Corresponding authors
24

25 **Abstract**

26 Gram-negative bacteria possess a unique and complex cell envelope, composed of an inner
27 and outer membrane separated by an intermediate cell wall-containing periplasm. This
28 tripartite structure acts intrinsically as a significant biological barrier, often limiting the
29 permeation of anti-infectives, and so preventing such drugs from reaching their target.
30 Furthermore, identification of the specific permeation-limiting envelope component proves
31 difficult in the case of many anti-infectives, due to the challenges associated with isolation of
32 individual cell envelope structures in bacterial culture. The development of an *in vitro*
33 permeation model of the Gram-negative inner membrane, prepared by repeated coating of
34 physiologically-relevant phospholipids on Transwell[®] filter inserts, is therefore reported, as a
35 first step in the development of an overall cell envelope model. Characterization and
36 permeability investigations of model compounds as well as anti-infectives confirmed the

37 suitability of the model for quantitative and kinetically-resolved permeability assessment, and
38 additionally confirmed the importance of employing bacteria-specific base materials for more
39 accurate mimicking of the inner membrane lipid composition - both advantages compared to
40 the majority of existing *in vitro* approaches. Additional incorporation of further elements of
41 the Gram-negative bacterial cell envelope could ultimately facilitate model application as a
42 screening tool in anti-infective drug discovery or formulation development.

43

44 Keywords: Gram-negative bacterial cell envelope, permeation kinetics, permeability
45 investigations, *in vitro* permeation model

46

47 CL cardiolipin

48 ER electrical resistance

49 IM inner membrane

50 KRB Krebs-Ringer buffer

51 LC liquid condensed

52 LE liquid expanded

53 MIC minimal inhibitory concentration

54 OM outer membrane

55 PC phosphatidylcholine

56 PL phospholipid

57 P_{app} apparent permeability coefficient

58 PBS phosphate buffered saline

59 PMB polymyxin B

60 POPE 1-hexadecanoyl-2-(9Z-octadecenoyl)-*sn*-glycero-3-phosphoethanolamine

61 POPG 1-hexadecanoyl-2-(9Z-octadecenoyl)-*sn*-glycero-3-phospho-(1'-*rac*-glycerol)

62	PVPA	phospholipid vesicle-based permeation assay
63	SE	standard error of the mean
64	SEM	scanning electron microscopy
65	UHPLC	ultra-high performance liquid chromatography

66

67

68

69

70

71

72

73

74

75

76

77

78

79

80

81

82

83

84

85

86 **1. Introduction**

87 The increasingly reported occurrence of multidrug-resistant bacteria, particularly those of the
88 Gram-negative classification, constitutes a growing threat to the state of health worldwide
89 [1,2]. The up-regulation and evolution of bacterial resistance mechanisms, leading to
90 inadequate drug levels at target sites, in fact acts to exacerbate the already challenging task of
91 successfully delivering anti-infective compounds or formulations into or across the cell
92 envelope [3]. The unique and complex structure of the Gram-negative bacterial envelope
93 operates intrinsically as a significant barrier, preventing the attainment of sufficient drug
94 levels at required sites of action in many instances [4,5]. The envelope itself consists of an
95 inner membrane (IM) of phosphatidylethanolamine, phosphatidylglycerol and cardiolipin as
96 principal phospholipid (PL) components, together with an asymmetric outer membrane (OM)
97 composed of a PL-containing inner leaflet and a lipopolysaccharide-containing outer leaflet.
98 These two membrane structures, additionally incorporating aspects of active transport, are
99 chiefly responsible for the intrinsic barrier properties of the envelope, which is therefore
100 commonly termed as a two-membrane barrier [6]. In addition however, the periplasmic space
101 separating the IM and OM serves as an area of high metabolic activity [7], and also houses the
102 peptidoglycan cell wall (a much thinner structure in comparison to Gram-positive bacteria).
103 The described intrinsic and resistance-compounded difficulties in achieving adequate drug
104 levels at bacterial target sites, together with the present low flow within the antibiotic
105 development pipeline, both contribute to a common inability to successfully treat Gram-
106 negative bacterial infections. Such difficulties can ultimately and collectively be regarded as
107 symptoms of a bacterial bioavailability problem [8], which is of vital importance to address.
108 The development of new anti-infective compound classes, the discovery of new targets, and
109 the advent of novel delivery strategies which facilitate effective anti-infective drug
110 penetration into or completely across the cell envelope (in order to reach intracellular sites of

111 action) therefore all constitute important areas of research in this respect. In addition, research
112 efforts within these areas require an increased understanding of and ability to investigate
113 bacterial permeation processes - a difficult task to achieve currently *in cellulo* due to
114 numerous associated challenges [8]. As such, a further research need to be addressed is the
115 requirement for models which allow for the characterization and quantification of anti-
116 infective permeation across the Gram-negative bacterial cell envelope. Such models would
117 provide complementary information to that obtained from established, '*in cellulo*' efficacy
118 testing approaches (such as determination of minimum inhibitory concentrations (MIC)),
119 allowing for optimization of drug candidates with respect to their target interaction as well as
120 their ability to sufficiently permeate the envelope barrier [9].

121

122 A variety of *in vitro* models in fact already exist for investigating interactions between anti-
123 infective compounds and bacterial cell envelope components; these can generally be classified
124 as electrophysiology models [10,11], Langmuir films [12] and vesicle-based assays [13].
125 While all such models are able to provide insight into bacterial permeation processes, they
126 also demonstrate several shortcomings. For instance, most focus on approximating the IM or
127 the OM alone, rather than both structures together (although some progress in this respect has
128 been recently made [14]). Furthermore, the PL composition of existing IM models often
129 deviates from that found in Gram-negative bacteria, in terms of either character or ratio [15].
130 The majority of the available approaches also do not allow for the quantification of
131 permeation processes [14, 16-18], an important ability which would allow for more in-depth
132 and accurate characterization of the way in which anti-infective compounds and formulations
133 interact with the bacterial envelope barrier [19]. Hence, there is a great need for new models
134 which represent the entire Gram-negative bacterial envelope with respect to both composition
135 and structure, and which are specifically designed to yield high content, quantitative
136 permeation information in a kinetically- and ultimately spatially-resolved manner.

137

138 As a first step in the production of an overall envelope model, this work is aimed at designing
139 and characterizing an *in vitro* model of the Gram-negative bacterial IM employing bacteria-
140 specific PLs, which is explicitly designed to quantify the passive permeation kinetics of anti-
141 infectives. A Transwell[®]-based setup, mimicking the conventional procedure to assess
142 permeation through mammalian cell barriers, was employed for the model preparation
143 process. An existing approach for production of lipid-based mammalian membrane models –
144 the phospholipid-vesicle based permeation assay (PVPA) [20] - was adapted in order to
145 prepare the bacterial IM model, utilizing a bacteria-specific lipid composition as found in the
146 IM of Gram-negative bacteria such as *Escherichia coli* and *Pseudomonas aeruginosa* [21].
147 The resulting preparation procedure was also employed to produce a model consisting solely
148 of phosphatidylcholine, as a major phospholipid in mammalian cell membranes [20]. The IM
149 model and the phosphatidylcholine-containing mammalian model (‘mammalian comparator’)
150 were then directly compared at each stage of IM characterization and in subsequent
151 permeability studies. This comparison was made in order to discern any lipid-dependent
152 differences between the models in terms of structure and function, and in doing so, to clearly
153 demonstrate the need to adapt an already existing mammalian lipid-based model using
154 bacteria-relevant materials. Models were characterized with respect to the interfacial behavior
155 of their component lipids, as well as integrity and robustness, topography, and thickness.
156 Furthermore, sets of model compounds including anti-infectives were utilized to ultimately
157 assess the impact of model lipid composition on permeability behavior, and to highlight the
158 ability to obtain quantitative and kinetically-resolved permeation data.

159

160 **2. Material and methods**

161

162 *2.1. Materials*

163 1-hexadecanoyl-2-(9Z-octadecenoyl)-*sn*-glycero-3-phosphoethanolamine (POPE), 1-
164 hexadecanoyl-2-(9Z-octadecenoyl)-*sn*-glycero-3-phospho-(1'-*rac*-glycerol) (sodium salt)
165 (POPG) and 1,1',2,2'-tetra-(9Z-octadecenoyl) cardiolipin (sodium salt) (CL) purchased from
166 Avanti Polar Lipids Inc. (Alabaster, AL, USA) were used for the IM model preparation. Egg
167 phosphatidylcholine (PC, Lipoid E80) was kindly donated by Lipoid GmbH (Ludwigshafen,
168 Germany), and employed for the mammalian comparator model. Polycarbonate filters with a
169 pore size of 800 nm (Merck Millipore, Darmstadt, Germany) were used for liposome
170 extrusion. Commercially available cell culture inserts (Transwell[®] permeable supports 3460)
171 were obtained from Corning Inc. (Acton, MA, USA). Calcein, sodium fluorescein, rhodamine
172 123, rhodamine B, rhodamine B isothiocyanate, atenolol, metoprolol tartrate, timolol maleate,
173 nadolol, acebutolol hydrochloride and alprenolol hydrochloride (Sigma-Aldrich Co., St.
174 Louis, MO, USA) served as model drugs. Polymyxin B (PMB), minocycline hydrochloride
175 and ciprofloxacin hydrochloride (Sigma-Aldrich Co., St. Louis, MO, USA) were employed as
176 anti-infective agents. All reagents for ultra-high performance liquid chromatography
177 (UHPLC) were purchased from VWR (Radnor, PA, USA). All other chemicals and solvents
178 were of at least analytical grade.

179

180 2.2 Methods

181

182 2.2.1 Langmuir trough experiments

183 Surface pressure-area π -A measurements of lipid monolayers composed of pure bacteria-
184 relevant PLs (POPE, POPG, CL), their 70:20:10 weight mixture [21], or pure PC were
185 performed using a thermostated Langmuir film trough (775.75 cm², Biolin Scientific, Finland)
186 enclosed in a plexiglas box. Experiments were performed at 294 and 303 K (21±1 °C and
187 30±1 °C respectively). PLs were dissolved in a mixture of chloroform and methanol (9:1 v/v)
188 to form solutions of 1 x 10¹⁵ molecules/μl. These solutions were then used to spread PLs at

189 the air/buffer interface, following subphase cleaning by suction. After PL deposition, the
190 system was left for 15 min to allow complete evaporation of the organic solvents. Monolayer
191 compression was then performed at a speed of $5 \text{ \AA}^2 \cdot \text{molecule}^{-1} \cdot \text{min}^{-1}$. The results reported
192 are mean values of at least two measurements. The surface compressional moduli (K) of
193 monolayers were calculated from equation (1):

194

$$195 \quad K = -A \cdot \left(\frac{d\pi}{dA} \right) \quad (1)$$

196

197 where A is the PL molecular area (\AA^2), $d\pi$ the surface pressure change (mN/m) and dA is the
198 change in the molecular area.

199

200 *2.2.2 Model preparation*

201 Both the bacterial IM and the mammalian comparator model were produced by adapting the
202 PVPA approach [20]. Liposomes composed of bacteria- or mammal-relevant PLs were first
203 prepared via the lipid film hydration method [22]. Briefly, POPE, POPG and CL were used in
204 a 70:20:10 weight ratio, as a bacteria-specific PL mixture. PC was used as mammal-specific
205 PL. POPE, POPG and CL, or PC alone were dissolved in a mixture of chloroform and
206 methanol (3:1, 5 ml) in a round-bottom flask (250 ml). Organic solvents were then removed
207 under reduced pressure (1 h: 200 mbar, 30 min: 40 mbar; 70 °C (bacteria-specific PL
208 mixture); 55 °C (mammal-specific PL)) using a Rotavapor R-205 (BÜCHI Labortechnik
209 GmbH, Essen, Germany) in order to form a thin lipid film. Phosphate buffered saline (PBS;
210 adjusted to pH 7.4) containing ethanol (10% v/v) was used to rehydrate the lipid film to obtain
211 the liposome dispersions (6% w/v total lipids). Afterwards, liposomes were sonicated for 1 h
212 and subsequently extruded (10 times; at 70 °C in case of the bacteria-relevant liposomes and
213 55 °C in case of the mammal-relevant liposomes), using a Liposofast L-50 extruder (Avestin

214 Europe GmbH, Mannheim, Germany). Both IM and mammalian comparator models were
215 then prepared by three consecutive cycles of liposome addition (75 μ l each) onto filter
216 supports, followed by centrifugation (30 min, 1040 g; Hettich Rotina 420 R, Hettich GmbH,
217 Tuttlingen, Germany) and oven-drying (50 min, 50 °C), with a final freeze-thaw step (-80 °C,
218 20 min; 45 °C for 20 min).

219

220 *2.2.3 Liposome size and surface charge measurements*

221 The hydrodynamic diameter and size distribution of liposomes was measured in PBS
222 (adjusted to pH 7.4) using dynamic light scattering, while surface charge (ζ -potential) was
223 determined (in the same medium) using laser doppler micro-electrophoresis (Zetasizer Nano
224 ZS, Malvern Instruments, UK).

225

226 *2.2.4 Confocal Raman microscopy*

227 Confocal Raman microscopy analysis was carried out to investigate the integrity of IM and
228 mammalian comparator model lipid coatings using a WITec alpha 300R+ imaging system
229 (WITec GmbH, Ulm, Germany), with an Olympus 50 x objective (N.A. 0.35). The excitation
230 source was a diode laser with a wavelength of 785 nm (50 mW). Models were analyzed
231 following preparation, and after 5 h incubation in Krebs-Ringer buffer (KRB) at 37 °C
232 without any further sample alteration. A confocal pinhole of 100 μ m rejected signals from
233 out-of-focus regions. Raman spectra were acquired every 100 μ m along the x- and y-axis
234 across the entire model membrane area, with an integration time of 4 s. Cosmic ray removal
235 and background subtraction were applied to all spectra, which were then processed using
236 hierarchical cluster analysis and basis analysis as multivariate methods for data processing,
237 and converted into spatially-resolved false-color images using WITec Project Plus software
238 (WITec GmbH, Ulm, Germany).

239

240 *2.2.5. Laser scanning interferometry*

241 Model topography was analyzed via a LEXT OLS4000 3D Laser Measuring Microscope
242 (Olympus AG, Tokyo, Japan), using a 405 nm semiconductor laser and a 20 x objective lens.
243 Transwell® membranes with PL coatings were cut out of the plastic Transwell® holder
244 surround and fixed on sample holders. Five representative membrane areas with an image size
245 of approximately 5.6 mm² each were analyzed. The center of the overall model surface was
246 denoted as area 1. The center of further imaged edge areas was set at a distance of 3000 µm
247 from the upper (2), right (3), bottom (4) and left (5) margin of the overall membrane surface.

248

249 *2.2.6 Scanning electron microscopy*

250 For scanning electron microscopy (SEM) investigations, freshly prepared model membranes
251 were first freeze-dried (Christ alpha 2-4 plus, Martin Christ Gefriertrocknungsanlagen GmbH,
252 Osterode am Harz, Germany). As for laser scanning interferometry, Transwell® membranes
253 with PL coatings were then cut out of the plastic holder surround; filter membranes were
254 subsequently removed. Vertical cross-sections of model membranes prepared using a scalpel
255 were then sputtered with gold, placed in a vertical manner on sample grids and subsequently
256 analyzed via SEM (Zeiss EVO HD 15, Carl Zeiss AG, Oberkochen, Germany).

257

258 *2.2.7. Permeability investigations*

259 For investigation of permeability behavior, transport studies were performed with at least 6
260 repetitions from 2 individual experiments. IM and mammalian comparator model-permeated
261 amounts of fluorescent dyes and β-blockers were determined, as model compounds. Amounts
262 of permeated ciprofloxacin and minocycline (with and without 1 h of model pre-incubation
263 with 15.4 µM PMB), as well as an AlexaFluor® 488-labeled functionalized fatty acid moiety
264 of the muraymycin A series of nucleoside antibiotics, together with corresponding reference

265 compound (both synthesized in-house according to Ries *et al.* [23]), were determined as anti-
266 infective substances.

267

268 Prepared model membranes on Transwell[®] filter inserts were placed in cell culture plates and
269 pre-incubated to rehydrate and equilibrate the system with pre-warmed KRB (pH 7.4, 37 °C)
270 for 30 min (upon which electrical resistance (ER) values were seen to stabilize, see
271 Supplementary Material). Following KRB removal, 520 µl of drug solution in KRB, in each
272 case at a concentration calculated in order to ensure sink conditions and adjusted to pH 7.4
273 (see Supplementary Material Tables S1 and S2, 1.27 µM in case of the functionalized fatty
274 acid moiety and reference compound) was added to the apical compartment of each culture
275 plate well (donor). A 1.5 ml volume of pre-warmed KRB was also added to the basolateral
276 compartment (acceptor). A 20 µl volume of drug solution in KRB was immediately removed
277 from the apical compartment, and employed to accurately measure the starting donor
278 concentration. Samples of 200 µl were taken from the basolateral compartment of culture
279 plate wells after 0, 0.5, 1, 1.5, 2, 2.5, 3.5 and 4.5 h, and used to quantify the permeated
280 amount of applied compounds (see below). The removed volume was replaced with an equal
281 volume of pre-warmed KRB in order to maintain sink conditions. Cell culture plates
282 containing coated Transwell[®] filter inserts were placed on an orbital shaker (IKA[®]-Werke
283 GmbH and Co KG, Staufen, Germany) set at 150 rpm and kept at 37 °C in an incubator for
284 the duration of transport studies.

285

286 *2.2.8. Quantification of permeated compound/drug amount and permeability calculations*

287 A Tecan Infinite[®] M200 plate reader (Tecan GmbH, Crailsheim, Germany) was used to
288 determine the permeated amount of fluorescent dyes (see Supplementary Material Table S1).

289 A Dionex Ultimate[®] 3000 UHPLC with an Accucore column (RP 18, 150 mm x 2.1 mm, 2.6
290 µm, Thermo Fisher Scientific Co., Waltham, MA, USA) was used to quantify the permeated

291 amount of β -blockers, ciprofloxacin and minocycline in transport studies. β -blocker
292 quantification was carried out using a binary solvent system (A = 36.6 mM Na₂HPO₄ + 33.4
293 mM triethylamine adjusted to pH 3; B = acetonitrile) as eluent in different ratios, depending
294 on the analyte; the flow rate and resulting compound retention time also varied (see
295 Supplementary Material Table S2). The column oven temperature in all cases was set to 40
296 °C. Ciprofloxacin and minocycline quantification was also carried out using a binary solvent
297 system (A= 0.02 M Na₂HPO₄ adjusted to pH 2.7; B= acetonitrile) as eluent in different ratios.
298 The resulting retention time also varied (see Supplementary Material Table S2). The column
299 oven temperature was set to 25 °C for ciprofloxacin and to 40 °C for minocycline. Permeated
300 amounts of AlexaFluor[®] 488-labeled fatty acid moiety and corresponding reference
301 compound were determined as described above for fluorescent dyes, with $\lambda_{exc.}$ (nm) = 470 and
302 $\lambda_{em.}$ (nm) = 520.

303

304 In all cases, the permeated compound amount was calculated in reference to calibration
305 curves created from samples of standard concentration. The cumulative permeated compound
306 amount was then plotted as a function of time. The slope of the linear region of this curve
307 constitutes the rate of compound flux, which was used to calculate the apparent permeability
308 coefficient (P_{app}) of each compound according to equation (2):

$$309 \quad P_{app} \text{ (cm/sec)} = J/(A \cdot c_0) \quad (2)$$

310

311 where J is the substance flux (mg/sec), A the surface area of the Transwell[®] filter insert (cm²)
312 and c_0 the initial compound concentration (mg/ml).

313

314 2.2.9. Statistical analysis:

315 Where appropriate, presented numerical data represent mean \pm standard error of the mean
316 (SE). Student's t-test was employed where relevant to evaluate significant differences ($*=P <$

317 0.05, ***= $P < 0.001$). All tests were calculated using the software SigmaPlot version 12.5
318 (Systat Software, Inc., San Jose, California, USA).

319

320 **3. Results and discussion**

321

322 *3.1. Bacterial IM and mammalian comparator membrane model preparation,*
323 *characterization and comparison*

324

325 *3.1.1. Interfacial behavior comparison of bacteria- and mammal-relevant phospholipids*

326 Prior to IM model development and optimization the interfacial behavior of individual
327 bacterial PLs, a bacterial PL mixture, and the mammal-specific PC was characterized using
328 the Langmuir trough technique. Surface pressure-area measurements of pure POPE, POPG
329 and CL monolayers were carried out, as well as the ternary mixture of POPE:POPG:CL in a
330 relevant 70:20:10 weight ratio were carried out to confirm miscibility of the bacterial PL
331 components. Investigation of PC lipid monolayers was also carried out in order to investigate
332 the occurrence of any notable differences in behavior of PC and the bacterial PL mixture at
333 the molecular level. Surface pressure-area isotherms were initially obtained at 21 °C, followed
334 by the more physiologically relevant temperature of 30 °C (representing the highest
335 temperature that could be applied in the experimental setup without the introduction of
336 inaccuracies caused by buffer evaporation) (Fig. 1A). Isotherms were then used to calculate
337 the compressibility moduli of PL monolayers (Fig. 1B).

338

339

340

341

342
343
344
345
346
347
348
349
350
351
352
353
354
355
356
357
358
359
360
361
362
363
364
365
366
367

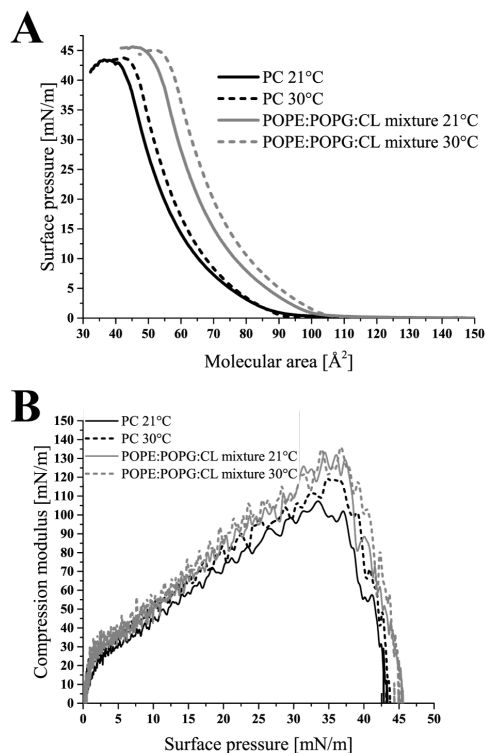


Fig. 1. Langmuir studies of bacterial IM and mammal-relevant PLs. Compression isotherms for bacteria-specific PL mixture (POPE:POPG:CL) and pure PC monolayers at 21 °C and 30 °C (A), showing differences in two-dimensional organization. Corresponding compressibility moduli as a function of surface pressure for both tested monolayers are additionally depicted (B), demonstrating the greater rigidity of the POPE:POPG:CL monolayer as compared to PC.

The isotherms obtained for the ternary bacterial PL mixture at 21 °C appeared to be intermediate between those of pure POPG and POPE (see Supplementary Material Fig. S1A), demonstrating that, although POPE is the major component of the ternary bacterial PL mixture, it is not the only mixture component contributing to the interfacial behavior. The influence of POPG and CL on the surface area-pressure measurements of POPE:POPG:CL monolayers, together with free energy of mixing and excess molecular area calculations (see Supplementary Material Fig. S1B, S1C) therefore implies the existence of a true lipid mixture. Comparison of the isotherms for the ternary mixture and pure PC monolayers revealed similar collapse pressures (π_c) at both 21 °C and 30 °C (Fig. 1A), with values around

368 44 mN/m (Table 1). However, the isotherm-derived larger molecular areas for the lipid
 369 mixture at pressure onset (A_{onset}) and collapse (A_c) account for more expanded monolayers of
 370 the ternary mixture compared to those of pure PC.

371
 372 **Table 1.** Summary of conducted Langmuir studies. Characteristic parameters of compression
 373 isotherms, comparing the bacteria-relevant POPE:POPG:CL mixture to PC at 21 °C and 30
 374 °C.

Applied		A_{onset}	A_c	π_c
Temperature (°C)	Monolayer	(Å ²)	(Å ²)	(mN/m)
21	POPE:POPG:CL	103.0	51.6	45.4
21	PC	97.5	43.5	42.9
30	POPE:POPG:CL	107.5	55.8	44.9
30	PC	92.3	45.4	43.5

382
 383 A_{onset} : molecular area at pressure onset, A_c : molecular area at collapse, π_c : surface pressure at
 384 collapse

385
 386 In addition to information gained directly from the isotherms, compressibility moduli were
 387 calculated in order to determine the physical state of the PC and PL mixture monolayers at
 388 various surface pressures. Compressibility moduli below 12.5 mN/m, in the range of 13-100
 389 mN/m, from 100 to 250 mN/m and above 250 mN/m infer a gaseous, liquid expanded (LE),
 390 liquid condensed (LC) and solid state of monolayers [24], respectively. PL organization at
 391 surface pressures in the range of 25-35 mN/m is of particular interest, as this represents the
 392 pressure range considered to correspond to the internal lateral pressure found in natural
 393 membranes [25]. PC monolayers were found to be in an LE state at 21 °C within this surface

394 pressure range, whereas POPE:POPG:CL monolayers appeared to be in the LC state. PC
395 monolayers were only observed to be in the LC state at higher surface pressures, from 30-38
396 mN/m (Fig. 1B). A similar observation was made from measurements performed at 30 °C. As
397 a result of this interfacial analysis, the bacterial PL mixture monolayer can be regarded as
398 being greater in molecular area and slightly more rigid compared to that of PC, at both
399 investigated temperatures; a first indication of differences in the behavior of bacteria- and
400 mammal-specific lipids on a molecular level can therefore be inferred.

401

402 *3.1.2. Bacterial IM and mammalian membrane model preparation*

403 Following initial Langmuir studies, membrane models consisting of the previously employed
404 POPE:POPG:CL in a 70:20:10 weight ratio (bacterial IM model) and pure PC (mammalian
405 comparator model) were prepared, via the PVPA approach [20]. In this two-step approach,
406 liposomes consisting of the PLs of interest are first prepared, as a means to facilitate lipid
407 deposition onto Transwell® filter supports without the use of organic solvents; liposomes are
408 then repeatedly coated onto filter supports in order to form a lipid membrane structure.
409 Although serving only as a means for lipid deposition, prepared POPE:POPG:CL and PC
410 liposomes were analyzed in terms of their hydrodynamic diameter and surface charge (ζ -
411 potential) in order to confirm a consistent outcome of liposome production. Low variation in
412 z-average and surface charge of both POPE:POPG:CL and PC liposomes confirmed the
413 acceptability of liposome preparation (see Supplementary Material Table S3), whereas
414 differences between bacterial and mammalian lipid liposomes (for instance with respect to
415 size) could be regarded as an outcome of the previous elucidated differences in PL packing
416 properties (see section 3.1.1).

417

418 While PVPA models consisting of PC alone have been previously established [26-28], the
419 primary objective of the current work was to develop a bacterial IM model. For this reason,

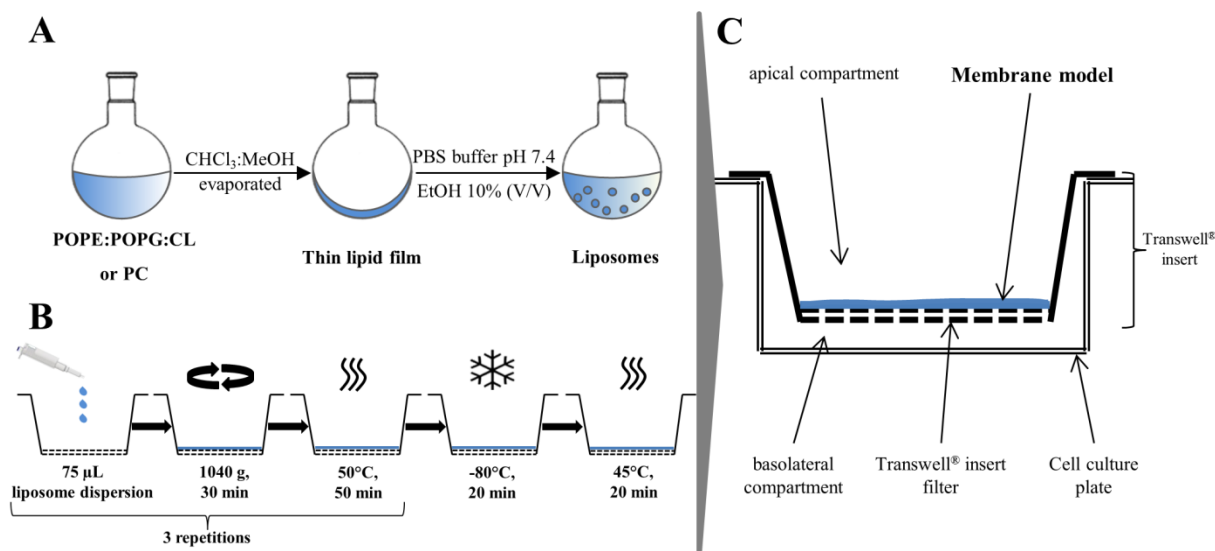
420 model preparation was adapted and optimized with respect to the use of POPE:POPG:CL.
421 The IM-optimized preparation procedure was then applied using PC liposomes in order to
422 produce a mammalian model which was truly comparative in nature. The procedure applied to
423 deposit and coat liposomes on a Transwell® filter was required to result in the construction of
424 an IM surrogate exhibiting robust permeation barrier properties, as well as a high level of
425 stability on exposure to buffer (as would occur during transport studies). Thus, the model
426 preparation procedure was optimized to fulfil these requirements. Deposition and coating
427 parameters were refined by tracking the impact of parameter alterations on model barrier
428 function in simulated transport experiments (entailing exposure to KRB, pH 7.4, 37 °C, for 5
429 h). Barrier properties of the IM model were inferred from measurement of ER, a common
430 means of monitoring barrier integrity in both cell-based [29,30] as well as cell-free [20]
431 permeation models (See Supplementary Material Figure S2).

432

433 The optimized preparation procedure (Fig. 2) consisted of three consecutive cycles of
434 liposome addition to a Transwell® filter insert, centrifugation and drying, followed by a final
435 freeze-thaw step – this step has been shown to promote liposome fusion, leading to a
436 confluent PL coating (rather than layers of discrete liposomes) with stable barrier function
437 [26]. The bacterial IM model constructed via this procedure showed sufficiently high and
438 constant ER values throughout a 5 h period of exposure to KRB (see Supplementary Material
439 Fig. S2), with no visible detachment of lipid coating from the Transwell® filter support. The
440 described preparation procedure as optimized for IM model preparation was then used for
441 preparation of a mammalian comparator model, by coating with PC liposomes. The
442 comparator model also demonstrated a high and stable level of ER upon incubation with KRB
443 (data not shown), as well as a lack of visible detachment from the Transwell® filter support.

444

445



446 **Fig. 2.** Model preparation procedure. Schematic of the two-step PVPA model preparation
 447 procedure, consisting of liposome preparation (A) and subsequent coating with liposome
 448 dispersions to form IM and mammalian comparator models (B). Liposomes consisting of
 449 POPE, POPG and CL were used to construct the bacterial IM model, while PC liposomes
 450 were employed to prepare the mammalian comparator. The final set-up of a model (blue)
 451 placed on top of a Transwell® filter support is additionally shown (C).

452

453 3.1.3. Model integrity and topography assessment

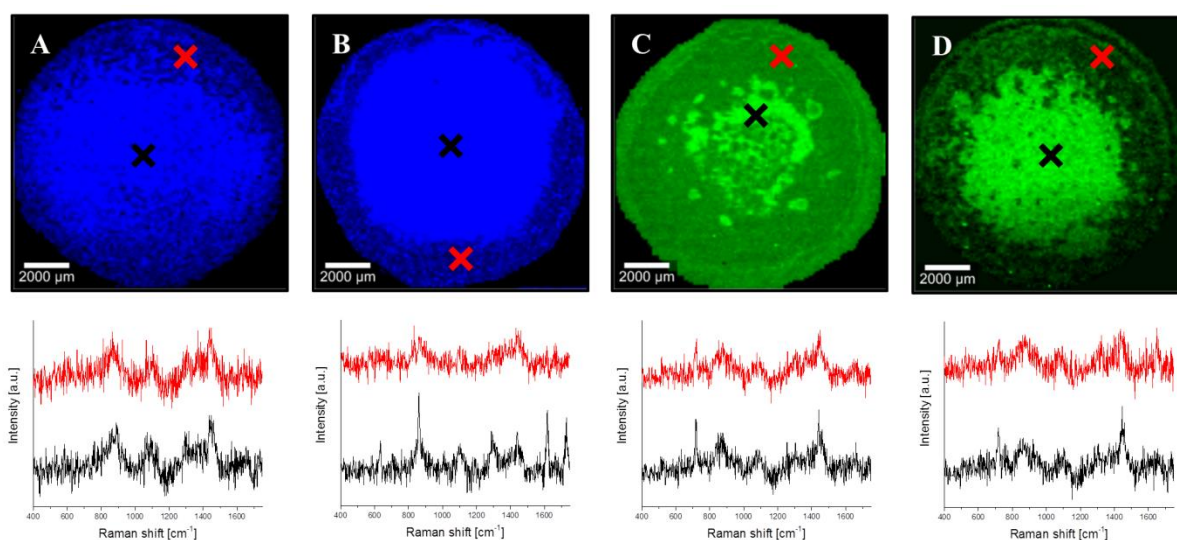
454 As described above, the optimized preparation procedure was seen in both the case of the IM
 455 and mammalian comparator model to result in a stable and robust membrane structure with
 456 appreciable barrier function. These properties can themselves be taken as an indication of a
 457 continuous and uninterrupted coating of bacteria- or mammal-specific lipids on Transwell®
 458 filter inserts. However, as any discontinuity present initially in the membrane structure or
 459 developing during transport experiments has the potential to lead to overestimation of the
 460 permeated amount of tested compounds/drugs and so distortion of resulting permeability data,
 461 it was deemed necessary to further investigate and firmly establish model integrity.
 462 Chemically selective analysis of the entire surface area of Transwell® filter inserts
 463 accommodating either the IM or mammalian comparator model was therefore performed

464 using confocal Raman microscopy, to determine model integrity following preparation as well
465 as following incubation in buffer (as described above for simulated transport studies). Due to
466 the structured surface of the models, optical topography was applied prior to confocal Raman
467 microscopy experiments in order to adjust the focus according to the sample topography, and
468 to characterize topography of the overall model area. Topography profiles indicated a higher
469 surface height at the edges compared to the center in the case of both models (see Supporting
470 Information Figure S3). This was expected due to the model preparation procedure, and is in
471 agreement with previous investigations [31].

472

473 Confocal Raman microscopy as such allows for label-free discrimination between the
474 polyester material of the Transwell[®] filter inserts and the PLs of the membrane models, based
475 on the individual spectra of the compounds. Consequently, the method allows for
476 determination of the extent to which Transwell[®] filter inserts are covered with model PLs.
477 Recorded Raman spectra were processed and subsequently converted into spatially-resolved
478 false color images, in order to enable visualization of the integrity of lipid coating (Fig. 3,
479 bacteria-relevant lipids of the IM model in blue, mammal-relevant lipids of the comparator
480 model in green). Continuous bacterial PL coverage of Transwell[®] filter inserts was observed
481 directly after IM model preparation, with no sign of coating defects (Fig. 3A); this continuous
482 lipid coating was seen to remain entirely intact following 5 h incubation of the IM model in
483 transport buffer (Fig. 3B). Likewise, the mammalian comparator model showed a continuous
484 coverage and the absence of any defects in the PL layer immediately following preparation
485 (Fig. 3C). Furthermore, no lipid-free Transwell[®] areas were observed following simulated
486 transport experiments (Fig. 3D). Even though variations in Raman signal intensity translating
487 to color intensity gradients could be observed in some images (especially Fig. 3D), overall
488 intact PL coverage was confirmed by the presence of lipid-specific peaks over the entire
489 Transwell[®] filter area in both models, before and after exposure to KRB. For illustration, the

490 individual raw Raman spectra derived from the central as well as from the outer region of
491 coated filter membranes (marked by black and red crosses respectively) are presented below
492 each of the Raman images in Fig. 3. The confirmed integrity of both the bacterial IM and
493 mammalian comparator models, together with the earlier demonstrated appropriate and stable
494 model barrier properties, therefore indicates the feasibility of compound permeability
495 determination in the IM and comparison with the mammalian comparator.



496 **Fig. 3.** Integrity assessment of the IM and mammalian comparator model. False color images
497 with representative single Raman spectra of central and outer regions of coated Transwell®
498 filter inserts, showing the IM model with bacteria-relevant lipids indicated in blue before (A)
499 and after (B) exposure to KRB, as well as mammal-relevant lipids of the comparator model in
500 green before (C) and after (D) exposure to buffer. The presence of lipid-specific Raman peaks
501 in all single Raman spectra at 1440 cm^{-1} (in raw state without any further spectral
502 manipulation, e.g. smoothing or subtraction) confirmed the overall lipid coverage. Color
503 intensity differences represent the variation in Raman signal intensity, not a lesser degree of
504 lipid coverage.

505
506 Having established that both the bacterial IM and mammalian comparator model were
507 suitable for permeability investigations, the focus of further characterization shifted towards

508 comparison and contrast of model properties. Following initial optical topography
509 investigations, laser scanning interferometry was employed to obtain more detailed insights
510 into the topographical profiles of both the IM and mammalian comparator model following
511 preparation. Hence, the bacterial IM model surface was analyzed at five representative
512 positions (center; upper, right, bottom and left edges) each with an approximate image size of
513 5.6 mm^2 , representing the maximum image size of the employed objective (Fig. 4A). A lower
514 height maximum of approximately $73 \text{ }\mu\text{m}$, as well as a more uniform surface profile were
515 found at the center of the IM model (Fig. 4B 1) as compared to the edge areas, which showed
516 height maximums of up to $184 \text{ }\mu\text{m}$ (Fig. 4B 2-5). The mammalian comparator model
517 exhibited a similar contrast in surface height maximums and profile uniformity when
518 comparing center and edge areas (Fig. 4C 1-5), indicating no marked differences in initial
519 topography of IM and mammalian comparator models.

520

521

522

523

524

525

526

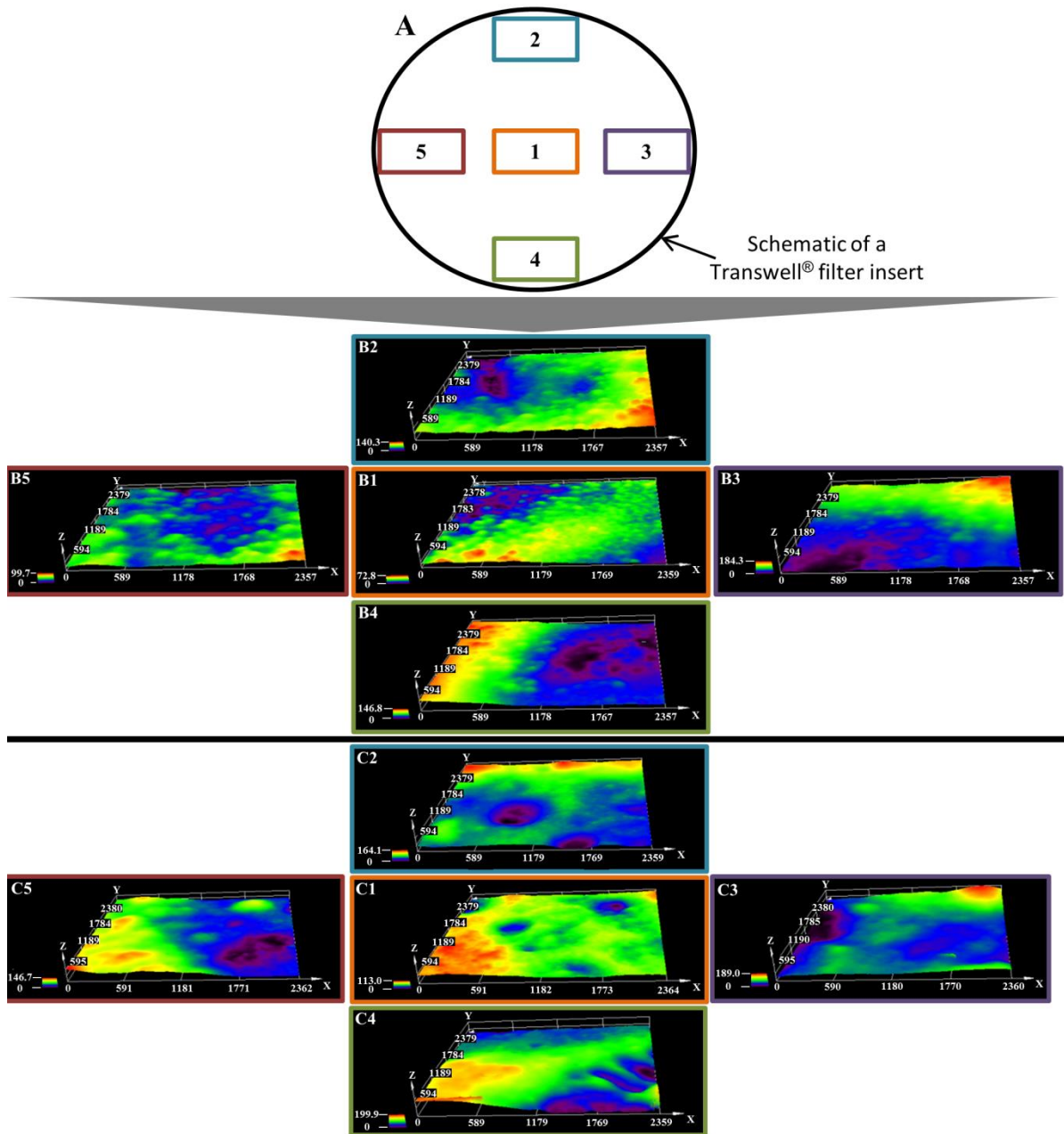
527

528

529

530

531



532 **Fig. 4.** Surface topography assessment of the IM and mammalian comparator model.
 533 Schematic of the model surface showing the location of the representative imaged areas (A).
 534 Topography of the bacterial IM model imaged at the five representative model areas (center
 535 (B1), as well as upper (B2), right (B3), bottom (B4) and left (B5) edges) is shown. The same
 536 areas of the mammalian comparator model (center (C1), upper (C2), right (C3), bottom (C4)
 537 and left (C5) edges) were additionally imaged.

538

539

540

541 3.1.4. Model thickness assessment

542 Model thickness constitutes another parameter which potentially affects the permeability
543 behavior of tested compounds/drugs [32]. Therefore, further to confirming model integrity
544 and an absence of drastic differences in surface topography, it had to be ensured that the IM
545 and the mammalian comparator model exhibited comparable values in the z dimension.
546 Freeze-dried, vertical cross-sections of both models were therefore applied in their original
547 orientation on sample grids and subsequently imaged and sized using SEM. Analysis of SEM
548 images revealed similar thicknesses of the IM and the mammalian comparator model, with
549 values of approximately 160 μm in both cases (Fig. 5). SEM images additionally indicated
550 differences in inner model morphology, potentially occurring as a result of the differences in
551 employed PLs; this indication was further confirmed by cryo-SEM analysis of IM and
552 mammalian comparator models (see Supplementary Material Figure S4).

553

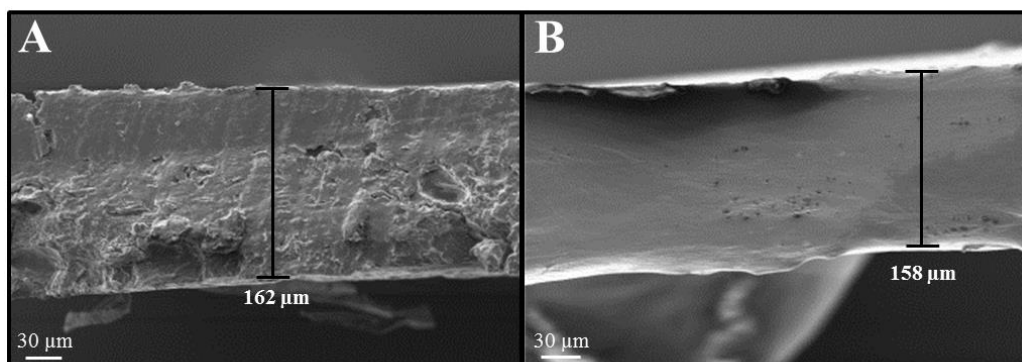
554

555

556

557

558



559 **Fig. 5.** Thickness evaluation of the IM and mammalian comparator model. Representative
560 SEM images of vertical cross sections of the bacterial IM (A) and mammalian comparator
561 model (B) without underlying Transwell[®] filter, indicating similarity in model thickness
562 (Images are representative of n=3 investigations, with mean values of $156 \pm 18 \mu\text{m}$ and $165 \pm$
563 $6 \mu\text{m}$ for the IM and mammalian comparator model respectively).

564

565

566 3.2 Evaluating the impact of model lipid composition on the permeability behavior of
567 compounds/drugs

568 The characterization measures employed in previous sections confirmed the suitability and
569 robustness of the bacterial IM model for transport studies, as well as the mammalian model as
570 a relevant comparator. Bacterial IM and mammalian comparator models prepared using the
571 same standardized procedure showed a required similarity in properties such as thickness, yet
572 demonstrated some degree of variation on both the molecular and microscale, as a function of
573 the different employed PLs. Whether such PL-dependent variations translated into differences
574 in permeability behavior in the IM and the mammalian comparator model was then further
575 investigated, to discern the importance and necessity of producing a bacterial IM model
576 specifically employing bacterial lipids in a physiologically relevant ratio.

577
578 A set of readily-quantifiable fluorescent dyes exhibiting a range of distribution coefficients at
579 pH 7.4 ($\log D_{(pH\ 7.4)}$) was utilized in a first step in order to conduct a preliminary proof of
580 concept study (see Supplementary Material Table S1). Point-wise differences in P_{app} values of
581 such compounds in the IM and the mammalian comparator were noted, showing a trend for
582 greater compound permeation across the IM model (Fig. 6A). This was seen to occur even in
583 case of the negatively charged dyes calcein and fluorescein, which could potentially have
584 been predicted to interact with negatively charged PLs (such as POPG and CL of the IM) in a
585 repulsive way, resulting in a low level of permeation [33]. Following this encouraging
586 preliminary result, it was decided to test a set of compounds which also varied in lipophilicity,
587 but which showed a much greater similarity with respect to other physicochemical parameters
588 (Table 2). For this purpose β -blockers were selected, as a standard compound set frequently
589 employed in cell- [34] and lipid-based [35,36] *in vitro* models for determination of
590 discriminatory capabilities. Utilizing this set of compounds additionally allowed for
591 permeability comparisons of the original PC-containing PVPA model with the current

592 mammalian comparator, further confirming its appropriateness to serve as a reference model
593 in the current work (see Supplementary Material Figure S5).

594

595 **Table 2.** Important physicochemical parameters of employed β -blockers.

β -blocker	$\log D_{(\text{pH } 7.4)}^{\text{a)}$	M_w (g/mol)	PSA (\AA^2) ^{b)}	H-bond donors/acceptors ^{b)}
Atenolol	-1.29	266.3	94.6	3 / 4
Metoprolol	-0.16	267.4	58.4	2 / 4
Timolol	0.03	316.4	85.2	2 / 8
Nadolol	0.68	309.4	88.8	4 / 5
Acebutolol	0.83	336.4	92.8	3 / 5
Alprenolol	1.38	249.3	43.7	2 / 3

596

PSA: polar surface Area

597

^{a)} Values from Zhu *et al.*[37])

598

^{b)} Values from Pubchem

599

600 Pair-wise comparisons of β -blocker permeability data again revealed significant point-wise
601 differences in P_{app} values (Fig. 6B), with a higher degree of permeation noted in the case of
602 the IM model in contrast to the mammalian comparator across the entire tested range of
603 compound lipophilicities. This observation further confirms the impact of model lipid
604 composition on compound permeability behavior.

605

606

607

608

609

610

611
612
613
614
615
616
617
618
619
620
621
622
623
624
625
626
627
628
629
630
631
632
633
634
635

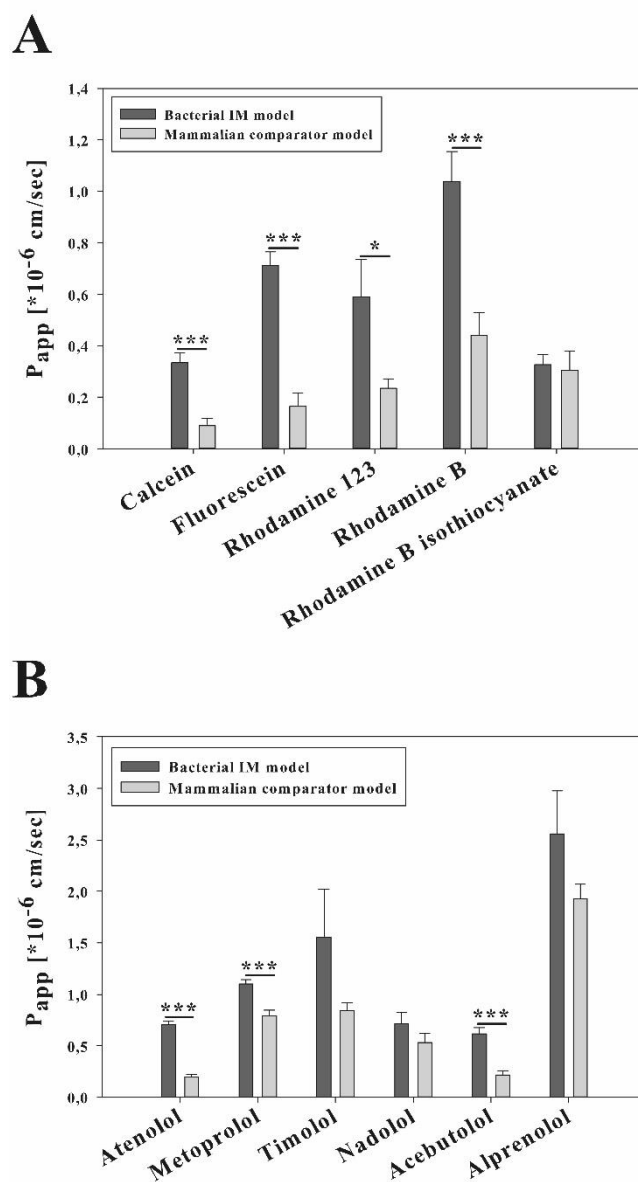


Fig. 6. Permeability experiment results of model compounds. P_{app} values of fluorescent dyes (A) and β -blockers (B), both in order of increasing lipophilicity, in the bacterial IM and mammalian comparator model. Values represent mean \pm SE; $n \geq 9$ from 3 individual experiments; *= $P < 0.05$, ***= $P < 0.001$.

636 3.3 Permeation and interaction of anti-infectives with the IM model in comparison to the
637 mammalian comparator model

638 The assessment and comparison of model compound permeability in the IM and mammalian
639 comparator model demonstrated an impact of the PL composition on compound permeation.
640 It was then further investigated whether this also applies in the case of anti-infective
641 compounds. Ciprofloxacin and minocycline, antibiotics from two different classes which need
642 to cross the IM to reach their target [38], were therefore tested and compared in both models.
643 The results again revealed significant differences in P_{app} values, with both antibiotics
644 permeating across the IM model to a greater extent than the mammalian comparator (Fig.
645 7A). The employment of bacteria-specific lipids in a permeation model of the IM (as well as
646 in further bacterial envelope model development) is therefore deemed to be of great
647 importance, in order to avoid underestimation of compound permeability - a problem which
648 could be even further exacerbated when additional permeation barriers of the bacterial cell
649 envelope (such as the OM) are taken into account.

650
651 In a further step, an additional antibiotic, PMB, was employed in conjunction with either
652 ciprofloxacin or minocycline, in order to investigate the existence of functional similarity
653 between the bacterial IM model and the Gram-negative bacterial inner membrane itself. PMB
654 is known to interact in an electrostatic manner at *in cellulo* assay concentrations [39] with
655 acidic PLs such as POPG and CL, as found in the Gram-negative bacterial inner membrane
656 [40,41]; this interaction is followed by insertion into the membrane structure, pore formation
657 and subsequent weakening of the membrane barrier function. In contrast, at similar PMB
658 concentrations, no such interaction and disruption is observed with membranes containing
659 overall electroneutral PLs like PC [40], as present in the mammalian comparator model. As a
660 result of its permeabilizing effect on the Gram-negative inner membrane, PMB may be used
661 clinically in a combination therapy approach together with other antibiotics such as the

662 currently employed minocycline [42,43], in order to provide enhanced cytoplasmic entry and
663 target access. To determine whether this scenario was reflected in the current *in vitro*
664 approach, both models were incubated with PMB in a relevant *in cellulo* assay concentration,
665 as previously shown to affect the IM of *Escherichia coli* [40]. Ciprofloxacin or minocycline
666 were then applied to the models, and compound permeation was again assessed. Both
667 ciprofloxacin and minocycline showed significantly higher P_{app} values in the IM model
668 following PMB treatment (Fig. 7B), whereas no significant difference in P_{app} was noted for
669 either antibiotic in the mammalian comparator model as a result of incubation with PMB (Fig.
670 7B). The observed permeabilization of the IM model (and corresponding lack of effect in the
671 mammalian comparator model) confirms a functional similarity of this structure to the Gram-
672 negative bacterial inner membrane. This study therefore provides a clear example of the
673 superior capacity of the bacterial IM model for evaluation of anti-infective permeation, further
674 highlighting the importance of employing bacteria-specific lipids in model development.

675

676

677

678

679

680

681

682

683

684

685

686

687
688
689
690
691
692
693
694
695
696
697
698
699
700
701
702
703
704
705
706
707
708

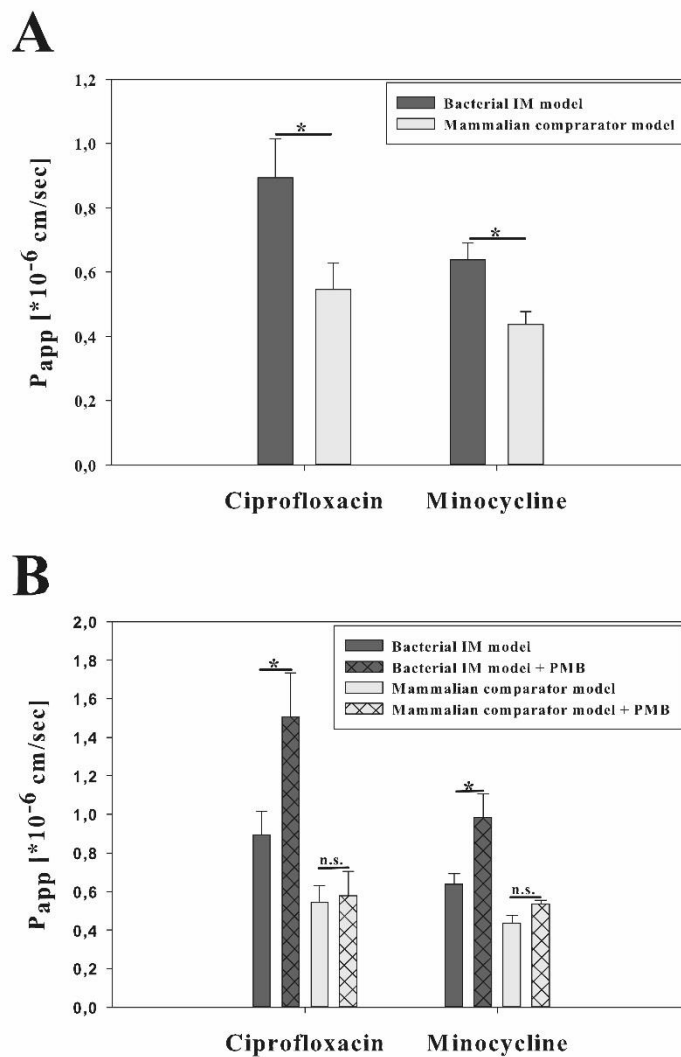


Fig. 7. Permeability experiment results of anti-infectives. P_{app} values of ciprofloxacin and minocycline in the bacterial IM and mammalian comparator model are shown (A), and are compared with P_{app} values following pre-incubation of both models with PMB (B). Values represent mean \pm SE; $n=6$ from 2 individual experiments; $*=P<0.05$, n.s. = not significant.

709 3.4 Comparison of the IM model to an established vesicle-based assay

710 Following clear demonstration of the advantage and need for the bacterial IM model, the IM
711 model permeation of an anti-infective-derived structure was investigated in a final, small scale
712 exploratory study, to allow for clear comparison of data obtained with the current model to
713 that derived from an established anti-infective permeation assay. In this respect, a
714 hydroxyguanidine-functionalized fatty acid moiety derived from the muraymycin A-series of
715 nucleoside antibiotics was chosen – this structure is proposed to account for the increased
716 activity of the A-series congeners in comparison to other muraymycins, due to its ability to
717 facilitate an increase in membrane permeability [44,45]. Recently, a simplified model system
718 was employed to experimentally validate this proposed. In this respect, the hydroxyguanidine-
719 functionalized fatty acid moiety, covalently linked to a fluorophore (AlexaFluor 488), was
720 applied in a vesicle-based *in vitro* model (not entirely utilizing bacteria-relevant PL
721 components) [23]. For comparison, a reference compound, lacking the hydroxyguanidine-
722 functionalized fatty acid motif, was employed. The functionalized fatty acid was observed to
723 permeate into lipid vesicles to a greater extent than the reference compound, assessed by
724 evaluating the fluorescence intensity inside vesicles relative to background; furthermore, the
725 functionalized fatty acid was seen to accumulate at the membrane interface right after the
726 addition of the compound to the immobilized vesicles [23]. However, it could not be
727 elucidated if this accumulation corresponded to a rapid permeation of the compound, due to
728 insufficient assay sensitivity.

729

730 In the current work, as for the previous vesicle-based study, the permeability of the ω -
731 hydroxyguanidinylated fatty acid conjugate was assessed in comparison to the reference
732 compound composed of the fluorescent label and linker alone (see Supplementary Material
733 Figure S6). Higher permeation rates as well as a significantly higher P_{app} value were found for
734 the functionalized fatty acid as compared to the reference compound in the bacterial IM

735 model (Fig. 8), confirming the previous findings of the vesicle-based assay [23]. A further
736 very notable result from the kinetically-resolved data as shown in Fig. 8A is the high
737 permeated amount of the functionalized fatty acid conjugate at 0 h. This observation strongly
738 suggests that the previously noted rapid accumulation effect does seem to correlate with
739 immediate membrane permeation, followed by a second permeation phase. This two-phase
740 model for the permeation of the functionalized fatty acid conjugate could only be derived
741 from kinetically-resolved data as facilitated by use of the IM model, thus further highlighting
742 the relevance of this new approach.

743

744

745

746

747

748

749

750

751

752

753

754

755

756

757

758

759
760
761
762
763
764
765
766
767
768
769
770
771
772
773
774
775
776
777
778
779
780
781
782
783
784

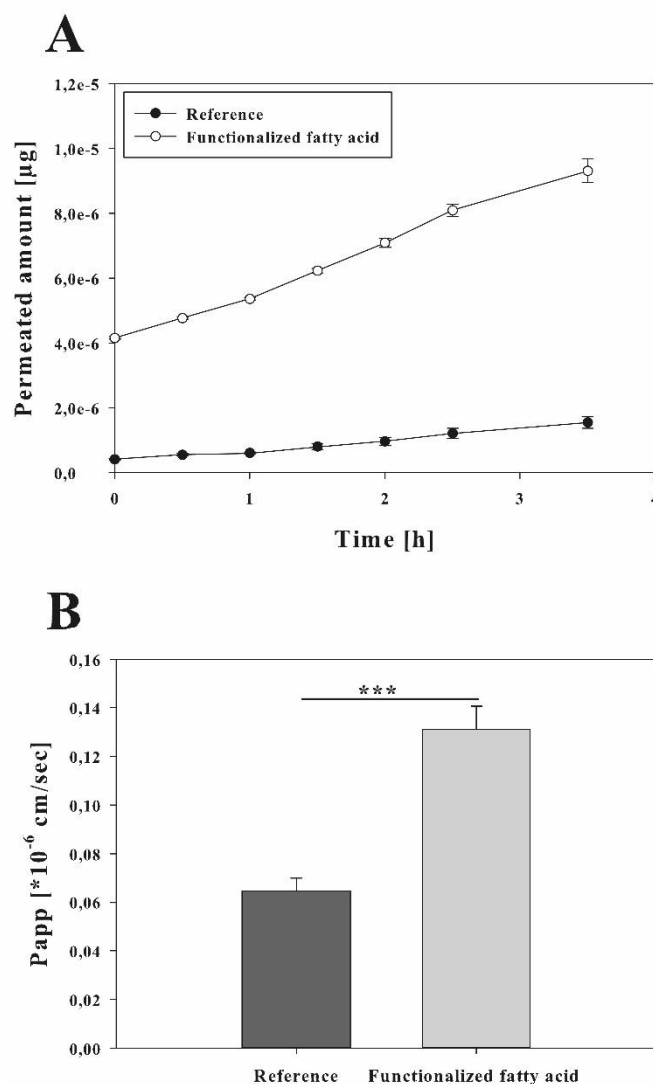


Fig. 8. Permeability experiment results of employed functionalized fatty acid moieties. Permeation rate and extent of the hydroxyguanidinylated fatty acid and reference compound (A), showing a permeability enhancing effect of the functionalized fatty acid moiety. The finding is also reflected in the calculated P_{app} values (B), additionally highlighting the advantage of the IM model for quantification of permeation processes and assessment of the permeation kinetics of tested compounds. Values represent mean \pm SE; $n=9$ from 3 individual experiments; ***= $P<0.001$.

785 **4. Conclusion**

786 We herein report the successful development of a stable and robust *in vitro* permeation model
787 of the Gram-negative bacterial IM, composed of bacteria-relevant PLs in a physiological
788 ratio. Characterization of the IM model and its components from the molecular level to the
789 macroscale, and comparison with an identically-produced model created from mammal-
790 relevant PC indicated a number of PL-related model deviations. These deviations were
791 ultimately shown to translate to significant differences in permeability of both model
792 compounds as well as anti-infectives as a function of model PL composition. The ability of
793 the novel IM model setup to provide quantitative data regarding the rate and extent of
794 compound permeation was also demonstrated, facilitating a more accurate characterization of
795 compound permeation as well as more information-rich evaluation of drug delivery
796 approaches across the IM models. Future work focuses on the development of an OM model,
797 in a further step towards creating a relevant permeation model of the complete Gram-negative
798 bacterial cell envelope.

799

800 **Acknowledgements**

801 The authors acknowledge Christoph Pauly (Department of Material Science And Engineering,
802 Chair of Functional Materials, Saarland University) for his assistance in the laser scanning
803 interferometry analysis, and the Core Facility for Integrated Microscopy, Faculty of Health
804 and Medical Sciences, University of Copenhagen for the assistance in taking the cryo-SEM
805 images.

806

807 **Funding**

808 This research did not receive any specific grant from funding agencies in the public,
809 commercial, or not-for-profit sectors.

810

811 **References**

- 812 [1] E.M. Wellington, A.B. Boxall, P. Cross, E.J. Feil, W.H. Gaze, P.M. Hawkey, A.S.
813 Johnson-Rollings, D.L. Jones, N.M. Lee, W. Otten, C.M. Thomas, A.P. Williams, The role of
814 the natural environment in the emergence of antibiotic resistance in gram-negative bacteria,
815 *Lancet Infect. Dis.*, 13 (2013) 155-165.
- 816 [2] M. McKenna, Antibiotic resistance: the last resort, *Nature*, 499 (2013) 394-396.
- 817 [3] F.C. Tenover, Mechanisms of antimicrobial resistance in bacteria, *Am. J. Med.*, 119
818 (2006) 3-10.
- 819 [4] M. Thein, G. Sauer, N. Paramasivam, I. Grin, D. Linke, Efficient subfractionation of
820 gram-negative bacteria for proteomics studies, *J. Proteome Res.*, 9 (2010) 6135-6147.
- 821 [5] M.L. Nelson, Grier, M.C., Barbaro, S. E., and Ismail M. Y., Polyfunctional antibiotics
822 affecting bacterial membrane dynamics, *Anti-Infect. Agents Med. Chem.*, 8 (2009) 3-16.
- 823 [6] H.I. Zgurskaya, C.A. López, S. Gnanakaran, Permeability barrier of Gram-negative cell
824 envelopes and approaches to bypass it, *ACS Infect. Dis.*, 1 (2015) 512-522.
- 825 [7] T.J. Silhavy, D. Kahne, S. Walker, The bacterial cell envelope, *Cold Spring Harb.*
826 *Perspect. Biol.*, 2 (2010) a000414.
- 827 [8] F. Graef, S. Gordon, C.M. Lehr, Anti-infectives in drug delivery-overcoming the Gram-
828 negative bacterial cell envelope, *Curr. Top. Microbiol. Immunol.*, (2016) epub ahead of print
829 1-22.
- 830 [9] K. Takroui, H.D. Cooper, A. Spaulding, P. Zucchi, B. Koleva, D.C. Cleary, W. Tear, P.J.
831 Beuning, E.B. Hirsch, J.B. Aggen, Progress against *Escherichia coli* with the oxazolidinone
832 class of antibacterials: Test case for a general approach to improving whole-cell Gram-
833 negative activity, *ACS Infect. Dis.*, 2 (2016) 405-426.
- 834 [10] J.M. Pages, C.E. James, M. Winterhalter, The porin and the permeating antibiotic: a
835 selective diffusion barrier in Gram-negative bacteria, *Nat. Rev. Microbiol.*, 6 (2008) 893-903.
- 836 [11] E.M. Nestorovich, C. Danelon, M. Winterhalter, S.M. Bezrukov, Designed to penetrate:
837 time-resolved interaction of single antibiotic molecules with bacterial pores, *Proc. Natl. Acad.*
838 *Sci. U. S. A.*, 99 (2002) 9789-9794.
- 839 [12] J. van Weerd, M. Karperien, P. Jonkheijm, Supported lipid bilayers for the generation of
840 dynamic cell-material interfaces, *Adv. Healthcare. Mater.*, 4 (2015) 2743-2779.
- 841 [13] A.I. Kuzmenko, H. Wu, F.X. McCormack, Pulmonary collectins selectively permeabilize
842 model bacterial membranes containing rough lipopolysaccharide, *Biochemistry*, 45 (2006)
843 2679-2685.
- 844 [14] L.A. Clifton, S.A. Holt, A.V. Hughes, E.L. Daulton, W. Arunmanee, F. Heinrich, S.
845 Khalid, D. Jefferies, T.R. Charlton, J.R. Webster, C.J. Kinane, J.H. Lakey, An accurate in
846 vitro model of the *E. coli* envelope, *Angew. Chem., Int. Ed. Engl.*, 54 (2015) 11952-11955.
- 847 [15] D.I. Fernandez, A.P. Le Brun, T.H. Lee, P. Bansal, M.I. Aguilar, M. James, F. Separovic,
848 Structural effects of the antimicrobial peptide maculatin 1.1 on supported lipid bilayers, *Eur.*
849 *Biophys. J.*, 42 (2013) 47-59.
- 850 [16] T. Mach, P. Neves, E. Spiga, H. Weingart, M. Winterhalter, P. Ruggerone, M. Ceccarelli,
851 P. Gameiro, Facilitated permeation of antibiotics across membrane channels-interaction of the
852 quinolone moxifloxacin with the OmpF channel, *J. Am. Chem. Soc.*, 130 (2008) 13301-
853 13309.
- 854 [17] M. Luckey, H. Nikaido, Specificity of diffusion channels produced by lambda phage
855 receptor protein of *Escherichia coli*, *Proc. Natl. Acad. Sci. U. S. A.*, 77 (1980) 167-171.
- 856 [18] J.L. Gornall, K.R. Mahendran, O.J. Pambos, L.J. Steinbock, O. Otto, C. Chimere, M.
857 Winterhalter, U.F. Keyser, Simple reconstitution of protein pores in nano lipid bilayers, *Nano*
858 *Lett.*, 11 (2011) 3334-3340.
- 859 [19] K. Lewis, Antibiotics: Recover the lost art of drug discovery, *Nature*, 485 (2012) 439-
860 440.

861 [20] G.E. Flaten, A.B. Dhanikula, K. Luthman, M. Brandl, Drug permeability across a
862 phospholipid vesicle based barrier: a novel approach for studying passive diffusion, *Eur. J.*
863 *Pharm. Sci.*, 27 (2006) 80-90.

864 [21] R.M. Epan, R.F. Epan, Bacterial membrane lipids in the action of antimicrobial agents,
865 *J. Pept. Sci.*, 17 (2011) 298-305.

866 [22] A.D. Bangham, M.M. Standish, J.C. Watkins, Diffusion of univalent ions across the
867 lamellae of swollen phospholipids, *J. Mol. Biol.*, 13 (1965) 238-252.

868 [23] O. Ries, C. Carnarius, C. Steinem, C. Ducho, Membrane-interacting properties of the
869 functionalised fatty acid moiety of muraymycin antibiotics, *Med. Chem. Comm.*, 6 (2015)
870 879-886.

871 [24] J.T. Davies, E.K. Rideal, *Interfacial phenomena*, Academic Press, New York, 1963.

872 [25] D. Marsh, Lateral pressure in membranes, *Biochim. Biophys. Acta*, 1286 (1996) 183-
873 223.

874 [26] G.E. Flaten, H. Bunjes, K. Luthman, M. Brandl, Drug permeability across a phospholipid
875 vesicle-based barrier 2. Characterization of barrier structure, storage stability and stability
876 towards pH changes, *Eur. J. Pharm. Sci.*, 28 (2006) 336-343.

877 [27] G.E. Flaten, M. Skar, K. Luthman, M. Brandl, Drug permeability across a phospholipid
878 vesicle based barrier: 3. Characterization of drug-membrane interactions and the effect of
879 agitation on the barrier integrity and on the permeability, *Eur. J. Pharm. Sci.*, 30 (2007) 324-
880 332.

881 [28] S.M. Fischer, G.E. Flaten, E. Hagesaether, G. Fricker, M. Brandl, In-vitro permeability
882 of poorly water soluble drugs in the phospholipid vesicle-based permeation assay: the
883 influence of nonionic surfactants, *J. Pharm. Pharmacol.*, 63 (2011) 1022-1030.

884 [29] F. Leonard, E.M. Collnot, C.M. Lehr, A three-dimensional coculture of enterocytes,
885 monocytes and dendritic cells to model inflamed intestinal mucosa in vitro, *Mol. Pharm.*, 7
886 (2010) 2103-2119.

887 [30] C.I. Grainger, L.L. Greenwell, D.J. Lockley, G.P. Martin, B. Forbes, Culture of Calu-3
888 cells at the air interface provides a representative model of the airway epithelial barrier,
889 *Pharm. Res.*, 23 (2006) 1482-1490.

890 [31] S.P. Gantzsch, B. Kann, M. Ofer-Glaessgen, P. Loos, H. Berchtold, S. Balbach, T.
891 Eichinger, C.M. Lehr, U.F. Schaefer, M. Windbergs, Characterization and evaluation of a
892 modified PVPA barrier in comparison to Caco-2 cell monolayers for combined dissolution
893 and permeation testing, *J. Control. Release*, 175 (2014) 79-86.

894 [32] A. Avdeef, *Absorption and drug development: Solubility, permeability and charge state*,
895 Wiley, Hoboken, NJ, USA, 2012.

896 [33] A. Malkia, L. Murtomaki, A. Urtti, K. Kontturi, Drug permeation in biomembranes: in
897 vitro and in silico prediction and influence of physicochemical properties, *Eur. J. Pharm. Sci.*,
898 23 (2004) 13-47.

899 [34] A.M. Marino, M. Yarde, H. Patel, S. Chong, P.V. Balimane, Validation of the 96 well
900 Caco-2 cell culture model for high throughput permeability assessment of discovery
901 compounds, *Int. J. Pharm.*, 297 (2005) 235-241.

902 [35] M. Kansy, F. Senner, K. Gubernator, Physicochemical high throughput screening:
903 parallel artificial membrane permeation assay in the description of passive absorption
904 processes, *J. Med. Chem.*, 41 (1998) 1007-1010.

905 [36] A. Avdeef, The rise of PAMPA, *Expert Opin. Drug Metab. Toxicol.*, 1 (2005) 325-342.

906 [37] C. Zhu, L. Jiang, T.M. Chen, K.K. Hwang, A comparative study of artificial membrane
907 permeability assay for high throughput profiling of drug absorption potential, *Eur. J. Med.*
908 *Chem.*, 37 (2002) 399-407.

909 [38] R.E.W. Hancock, A. Bell, Antibiotic uptake into Gram-negative bacteria, in: G.G.
910 Jackson, H.D. Schlumberger, H.J. Zeiler (Eds.), *Perspectives in anti-infective therapy*,
911 Wiesbaden 1989, pp 11-29.

912 [39] R. Daugelavicius, E. Bakiene, D.H. Bamford, Stages of polymyxin B interaction with the
913 Escherichia coli cell envelope, *Antimicrob. Agents Chemother.*, 44 (2000) 2969-2978.
914 [40] D.R. Storm, K.S. Rosenthal, P.E. Swanson, Polymyxin and related peptide antibiotics,
915 *Annu. Rev. Biochem.*, 46 (1977) 723-763.
916 [41] M. Teuber, J. Bader, Action of polymyxin B on bacterial membranes. Binding capacities
917 for polymyxin B of inner and outer membranes isolated from Salmonella typhimurium G30,
918 *Arch. Microbiol.*, 109 (1976) 51-58.
919 [42] Y. Zhang, F. Chen, E. Sun, R. Ma, C. Qu, L. Ma, In vitro antibacterial activity of
920 combinations of fosfomicin, minocycline and polymyxin B on pan-drug-resistant
921 Acinetobacter baumannii, *Exp. Ther. Med.*, 5 (2013) 1737-1739.
922 [43] D.R. Bowers, H. Cao, J. Zhou, K.R. Ledesma, D. Sun, O. Lomovskaya, V.H. Tam,
923 Assessment of minocycline and polymyxin B combination against Acinetobacter baumannii,
924 *Antimicrob. Agents. Chemother.*, 59 (2015) 2720-2725.
925 [44] L.A. McDonald, L.R. Barbieri, G.T. Carter, E. Lenoy, J. Lotvin, P.J. Petersen, M.M.
926 Siegel, G. Singh, R.T. Williamson, Structures of the muraymycins, novel peptidoglycan
927 biosynthesis inhibitors, *J. Am. Chem. Soc.*, 124 (2002) 10260-10261.
928 [45] D. Wiegmann, S. Koppermann, M. Wirth, G. Niro, K. Leyrer, C. Ducho, Muraymycin
929 nucleoside-peptide antibiotics: uridine-derived natural products as lead structures for the
930 development of novel antibacterial agents, *Beilstein J. Org. Chem.*, 12 (2016) 769-795.
931
932
933
934